J Mater Sci (2006) 41:4405–4412
DOI 10.1007/s10853-006-0152-2

Interfacial structure in silicon nitride sintered with lanthanide oxide

C. Dwyer · A. Ziegler · N. Shibata · G. B. Winkelman · R. L. Satet · M. J. Hoffmann · M. K. Cinibulk · P. F. Becher · G. S. Painter · N. D. Browning · D. J. H. Cockayne · R. O. Ritchie · S. J. Pennycook

Received: 2 January 2006 / Accepted: 28 March 2006 / Published online: 14 May 2006

Abstract Three independent research groups present a comparison of their structural analyses of prismatic interfaces in silicon nitride densified with the aid of lanthanide oxide Ln_2O_3. All three groups obtained scanning transmission electron microscope images which clearly reveal the presence of well-defined Ln segregation sites at the interfaces, and, moreover, reveal that these segregation sites are element-specific. While some results differ across the three research groups, the vast majority exhibits good reproducibility.

Introduction

It has long been recognized that the room-temperature strength of monolithic Si_3N_4 ceramics depends strongly on the presence of defects, while the room-temperature fracture toughness is greatly influenced by the microstructure. Generally, fine-grained materials exhibit the highest strength, whereas high toughness is promoted by large-grained microstructures and an intergranular fracture path. While strength is commonly associated with flaw size (which is invariably related to grain size), toughness is generally attributed to dissipative mechanisms acting behind the crack tip, including grain bridging and frictional pull-out processes associated with elongated grains [1–18]. Consequently, a fine-grained microstructure containing a significant volume fraction of elongated grains, and one which exhibits intergranular fracture, generally provides both high toughness and good strength. Aside from the properties of the starting powder, grain growth in Si_3N_4 ceramics is known to be influenced mainly by the sintering additives and sintering conditions [19, 20]. On the other

C. Dwyer · G. B. Winkelman · D. J. H. Cockayne
Department of Materials, University of Oxford, Oxford OX1 3PH, UK
e-mail: dwyer@materials.ox.ac.uk

A. Ziegler · N. D. Browning · R. O. Ritchie
Materials Sciences Division, Lawrence Berkeley National Laboratory, Berkeley, California 94720, USA

N. Shibata
Institute for Engineering Innovation, University of Tokyo, Yayoi, Tokyo 113-8656, Japan

R. L. Satet · M. J. Hoffmann
Institut für Keramik im Maschinenbau, Universität Karlsruhe, Haid-und-Neu-Strasse 7, D-76131 Karlsruhe, Germany

M. K. Cinibulk
Materials and Manufacturing Directorate, Air Force Research Laboratory, Wright-Patterson Air Force Base, Ohio 45433, USA

P. F. Becher · G. S. Painter
Metals and Ceramics Division, Oak Ridge National Laboratory, Oak Ridge, TN 37831, USA

N. D. Browning
Department of Chemical Engineering and Materials Science, University of California, Davis, California 95616, USA

R. O. Ritchie
Department of Materials Science and Engineering, University of California Berkeley, Berkeley, California 94720, USA

S. J. Pennycook
Condensed Matter Sciences Division, Oak Ridge National Laboratory, Oak Ridge, TN 37831, USA

hand, the precise reasons why a ceramic fails intergranularly, as opposed to transgranularly, are still uncertain, although the predominant view is that debonding and crack advance along the boundaries is facilitated by ''weakened'' interfaces. If this view is correct, the interfacial strength, and hence the crack path, must be controlled by the chemical composition, atomic structure and bonding along the grain-boundary phase [21]. In silicon nitride ceramics, this grain-boundary phase is typically an amorphous silicon oxynitride phase containing the sintering additive. Hence, the sintering additive plays a rather complex role, since it can influence both grain growth and interfacial strength.

In the current work, independent research groups at the University of Oxford, Lawrence Berkeley National Laboratory (LBNL) and Oak Ridge National Laboratory (ORNL) present a comparison of their structural analyses [22–26] of prismatic interfaces in silicon nitride densified with the aid of lanthanide oxides Ln_2O_3 (Ln = La, Sm, Er, Gd, Yb, Lu). The majority of these ceramics (those containing La, Sm, Yb, and Lu) were prepared as part of a systematic investigation of the influence of rare-earth oxide sintering additives on the microstructural evolution and the resulting mechanical properties of silicon nitride [27, 28]. The structural analyses of the interfaces were conducted using (high-angle) annular dark-field (ADF) imaging, whereby Ln atoms are detected with great efficiency due to their large atomic number, and electron energy-loss spectroscopy (EELS) in the scanning transmission electron microscope (STEM). The first of these analyses was reported by the ORNL group [22], who obtained images showing La segregation at a prismatic interface, and compared the observed positions of La with predictions of density functional theory (DFT) calculations. A report from the LBNL group followed [23], demonstrating such segregation for various different Ln, in addition to EELS measurements of atomic bonding at the interface. An article was published by the Oxford group shortly thereafter [24], in which images of interfaces in La and Lu-containing ceramics were processed to obtain the projected coordinates of Ln atoms in the first and second cation layers. The Oxford group subsequently extended their work to obtain the three-dimensional coordinates of La and Lu [25]. Finally, a recent article published by the ORNL group [26] extends their earlier comparison of experimental observations and DFT calculations to include Gd and Lu.

In terms of their influence on microstructure, Ln_2O_3 sintering additives are known to significantly affect anisotropic grain growth [27, 28]. In contrast, most of the ceramics studied in the present work (those containing La, Sm, Yb, and Lu) were designed to have similar grain size distributions, so that the effects of the grain-boundary chemistry on the mechanical properties could be isolated [27]. For these ceramics, it was found that the fracture toughness increased with the ionic radius of the Ln [27]. As the influence of the grain size distribution on the fracture toughness was largely constant, the observed changes in fracture toughness were attributed to a weakening of the interfaces as the ionic radius of the Ln increased [27]. Hence, ceramics sintered with the aid of Ln_2O_3 form an interesting system in which to compare and discuss the relation between mechanical properties and atomic-scale observations of interfacial structure. While such discussion is beyond the scope of the present work (which focuses mainly on the results of the structural analyses themselves), the reader is referred to Refs. [22–26, 30] and references therein.

Experimental

Ceramics processing

The La, Sm, Gd, Yb and Lu-containing ceramics were prepared so as to have the same equivalent percent of each corresponding constituent species [26, 27]. To this end, powder batches of the five-component Si–Ln–Mg–O–N systems were prepared with the following oxide compositions in wt%: $7.2La_2O_3$–2.0MgO–$2.2SiO_2$, $7.7Sm_2O_3$–1.9MgO–$2.19SiO_2$, $7.97Gd_2O_3$–1.98MgO–$2.18SiO_2$, $8.6Yb_2O_3$–1.97MgO–2.17 SiO_2, and $8.7Lu_2O_3$–1.97MgO–$2.16SiO_2$. The powders were attrition milled using silicon nitride grinding media, and subsequently dried and sieved. Green bodies $65 \times 45 \times 7$ mm^3 were uniaxially and then cold isostatically pressed at 400 MPa. Samples were densified using a two-step sinter-HIP (hot isostatic pressing) technique [31] whereby closed porosity is achieved at low N_2 pressure during an initial sintering step, and full density is achieved during a subsequent HIP step at a maximum N_2 pressure of 10 MPa. For the samples containing La, Sm, Yb and Lu, the sintering conditions were different for each Ln, and chosen so as to achieve a comparable microstructure in all four samples (see [27] for details). The volume of each plate was sufficiently large that compositional fluctuations in the core of each sample, from where specimens were extracted, were minor.

The additional Yb and Er-containing material that was investigated at LBNL was prepared with a 2:1 molar ratio of SiO_2:Ln_2O_3 (taking into account the oxide present on the surface of the Si_3N_4 particles) placing the composition directly on the Si_3N_4–$Er_2Si_2O_7$ and Si_3N_4–$Yb_2Si_2O_7$ tie line, respectively. Care was taken in handling the Si_3N_4 powder so as to prevent additional oxidation. The composition was processed to obtain 12.3 vol% grain-boundary phase—the equivalent to a 15wt% $Y_2Si_2O_7$–Si_3N_4 material—which was found to sinter to greater than 99%

theoretical density. The material composition was prepared by milling the powder using Si_3N_4 milling media in anhydrous methanol. The dried powder was then sieved, and lightly die-pressed into a rectangular shape. The shape was then immediately cold isostatically pressed to obtain maximum green density and to minimize density gradients. The sample was placed in a bed of 30 wt% BN-Si_3N_4 powder in a BN-coated graphite crucible and sintered in a graphite-element furnace at 1850 °C for 4 h under 1.8 MPa of N_2.

TEM specimen preparation

Oxford

TEM specimens were prepared by either dimple grinding (Gatan Inc., Model 656) or wedge polishing (South Bay Technology, Inc., Model 590W), followed by two-stage ion beam thinning using beam energies of 4.0 and 2.5 keV (Gatan Inc., Model 691, and Fischione Instruments Inc., Model 1010). To prevent carbon contamination of the specimens under the electron beam, carbon coating was not employed. The specimens were plasma cleaned (Fischione Instruments Inc., Model 1020) immediately prior to insertion into the microscope.

LBNL

Specimens for examination in the TEM were prepared by grinding, dimpling, and ion milling. The low-voltage ion milling was performed with a LINDA ion mill (Technoorg LINDA, IV3H/L ion-beam thinning unit, Scientific Technical Development LTD., USA) to produce foils with a thickness of 10–15 nm and with highly smooth surfaces (surface roughness ≤1 nm). The specimens were slightly carbon coated to prevent charging when exposed to the electron beam in the TEM.

ORNL

The bulk material was mechanically polished to be about 50-μm thickness using a precision polishing system (Allied High Tech Products, Inc., TechPrep), and then dimpled (Gatan Inc., Model 656) to have a thickness less than 10 μm before ion thinning. In the ion-thinning process (Gatan Inc., Model 691), the initial accelerating voltage of Ar ions was 4.5 kV with an incident beam angle of 7°, and gradually decreased to 2 kV as thinning progressed. Finally, a low-voltage ion thinning (1 kV) was applied to remove any surface damage layers (Fischione Instruments Inc., Model 1010). A thin amorphous carbon film (~3 nm) was deposited on the sample to avoid charging effects.

STEM configurations

Oxford

ADF-STEM images were obtained using a JEOL 2200FS TEM/STEM operating at 200 kV, and fitted with aberration-correctors (CEOS GmbH) for the probe-forming and objective lenses. A probe convergence semi-angle of 16 mrad was used, providing a probe size of less than 0.16 nm. The inner and outer semi-angles of the (high angle) ADF detector were approximately 50 and 140 mrad, respectively. EELS was used to confirm the presence of lanthanide atoms in the intergranular films; a JEOL 3000F TEM/STEM equipped with an energy-loss spectrometer (Gatan, Inc.) was used for this purpose.

LBNL

Electron energy-loss spectra and ADF-STEM images were obtained with a monochromated FEI Tecnai F20 STEM operating at 200 kV. The lens conditions in the microscope were defined for imaging and spectroscopy with a probe size of 0.14 nm. The inner and outer semi-angles of the (high angle) ADF detector were chosen to be 74 and 110 mrad, respectively. All images were acquired with an objective semi-angle of 13.5 mrad. Energy-loss spectra were acquired with a collection semi-angle of 10 mrad. These experimental conditions are enough to minimize the effects of strain fields on the ADF image. In this experimental condition, the incoherent (high-angle) ADF image allows the structure of the grains to be directly observed, and the image can also be used to position the electron probe for EELS.

ORNL

Atomic-resolution images were taken with a VG Microscopes HB603U dedicated STEM operating at 300 kV, and equipped with aberration corrector (Nion Co.). A probe convergence semi-angle of approximately 22 mrad was used, providing a minimum probe diameter less than 0.1 nm, and (high-angle) ADF images were collected with a detector angle range of approximately 35–300 mrad. EELS and energy dispersive X-ray spectroscopy (EDS) were used to confirm the presence of lanthanide additives in the intergranular films and triple pockets; a Hitachi HD-2000 STEM was used for this purpose.

Results and discussion

Figure 1 shows representative ADF-STEM images of prismatic interfaces in silicon nitride densified with the aid of Ln_2O_3. These images are a small collection of those obtained

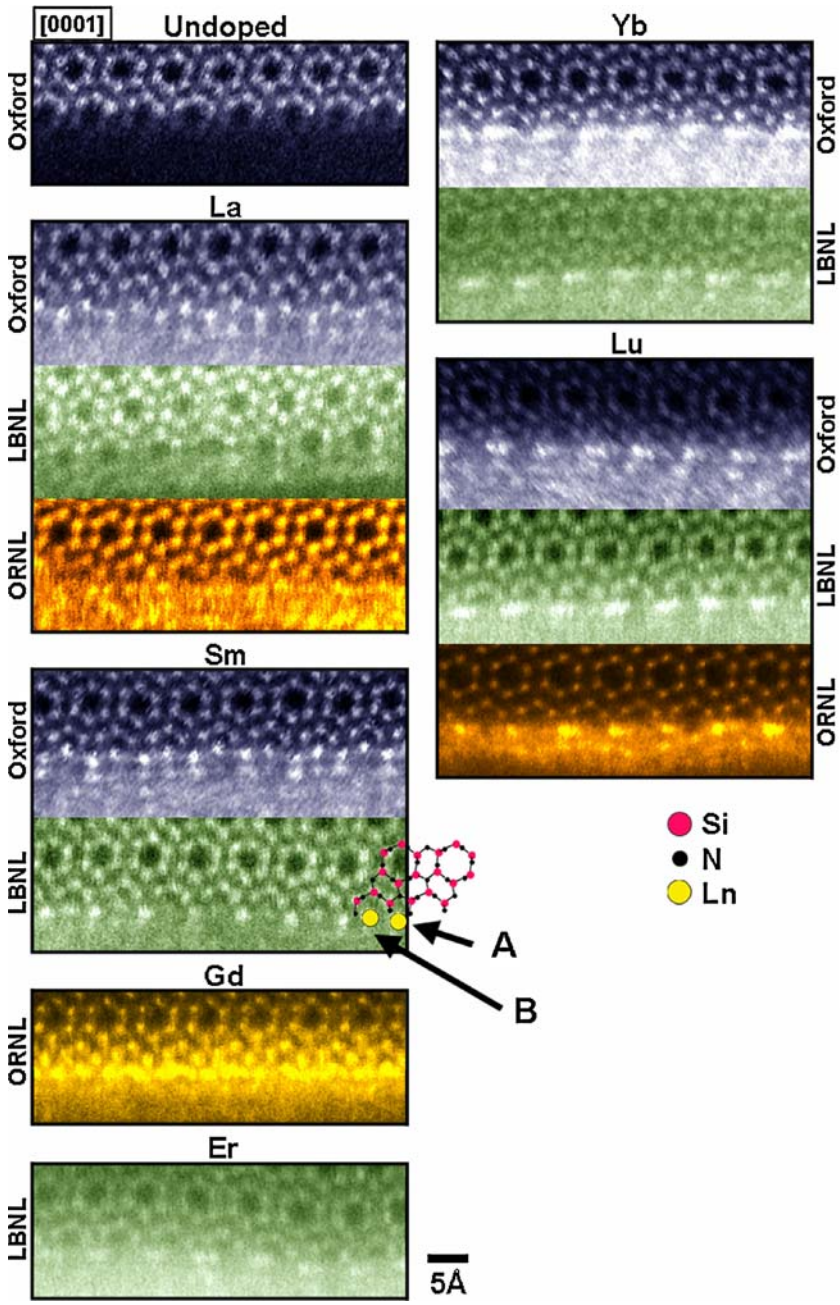

Fig. 1 ADF-STEM images of prismatic interfaces in various Ln-containing silicon nitride ceramics obtained by the research groups at Oxford, LBNL and ORNL. With the exception of the Yb-containing ceramic, adjacent images are of the same sample. An image of a prismatic interface in undoped silicon nitride is also shown for comparison

by the three research groups (Oxford, LBNL and ORNL). With the exception of the images of the Yb-containing material, adjacent images are of the same sample obtained by the different research groups. An image of a prismatic interface in silicon nitride densified *without* any sintering aid (undoped sample) is also shown for comparison.

The ADF-STEM images in Fig. 1 are representative of the atomic structures projected along the direction of the electron beam. In each image, a prismatic crystal-amorphous interface lies along the horizontal and is viewed edge-on. Above each interface is a Si_3N_4 grain oriented along the [0001] direction. Below each interface is amorphous silicon oxynitride. In this orientation, the Si_3N_4 structure consists of atomic columns parallel to the electron beam and containing either silicon or nitrogen (see the atomic model overlay in Fig. 1). In each image, the Si_3N_4 grain appears as an array of spots positioned at the vertices of hexagons, with each spot corresponding to a silicon column. Nitrogen columns, which are situated both amongst the silicon columns comprising each hexagon and at the mid-point of each hexagon triplet, are difficult to detect due to their lower atomic number. It is seen that the termination of the Si_3N_4 grains is atomically flat, and appears in the images as consisting of characteristic ''half-

hexagons'' of silicon columns. (At first, this termination is most easily seen in the image of the undoped sample.) In fact, although the anions are not directly visible, the geometry revealed by the images implies that the Si_3N_4 grains are anion terminated. The amorphous silicon oxynitride comprises, in some images, part of a thin intergranular film, and in other images, part of a triple pocket. Except in the image of the undoped sample, this amorphous phase appears bright due to the presence of Ln. However, because it is disordered, this amorphous phase produces no obvious atomic-scale contrast. In a manner strikingly different from the image of the undoped sample, the images of the Ln containing samples feature bright spots immediately below the Si_3N_4 grain. These bright spots correspond to Ln atoms which have segregated to the crystal–amorphous interface, and largely conform to the periodicity of the adjacent Si_3N_4 grain. In many images, a second, albeit less obvious, layer of Ln sites can be seen extending further into the amorphous phase.

Although the images in Fig. 1 were obtained by the different research groups, the vast majority of these images exhibits consistent results. More specifically, and perhaps most importantly, the images reveal that the Ln atoms attach to an anion-terminated Si_3N_4 grain, and that their positions at the interface are element specific. For example, in the images of the Sm sample (Oxford and LBNL), Sm occupies two well-separated sites (separation ≈ 0.35 nm) immediately adjacent to the Si_3N_4 grain. (For later purposes, these sites will be referred to as sites A and B, see the atomic model overlay in Fig. 1). In contrast, the images of the (two distinct) Yb samples (Oxford and LBNL) and the Lu sample (all three research groups) exhibit Ln sites lying much closer together, actually with an unphysical separation of approximately 0.15 nm. However, this is attributed to the Ln atoms being shifted relative to each other in the direction of the electron beam and therefore their projected separation appears very close. The close separation of the Yb and Lu sites means that they are sometimes unresolved and appear as one elongated site [24, 26], although the separation of Yb sites occasionally appears larger [23]. The images of the Gd and Er samples, each obtained by only one research group, exhibit Ln positions consistent with the above trends with respect to atomic number, i.e. Gd positions adjacent to the Si_3N_4 grain are similar to those of Sm, and Er positions are similar to those of Yb and Lu. While the vast majority of the images in Fig. 1 exhibit consistent results, those of the La-containing sample are exceptional and will be discussed below.

Another feature that is consistent among the images in Fig. 1 is that, with the exception of La, the Ln site A almost always appears brighter than site B. Given that the intensity in the ADF-STEM images is, with some exceptions, qualitatively interpretable in terms of the projected (squared) atomic number density in the specimen, the greater intensity at site A suggests a greater occupancy by Ln. This interpretation is also consistent with DFT calculations of Ln bonding to a nitrogen-terminated prismatic surface [26, Dwyer and Nguyen-Manh, Unpublished 2004], which predict that site A is the most stable Ln site. Hence, for low enough concentrations of Ln, it is expected that site A is more likely to be occupied than site B [26]. The consistency of the image features, mentioned in this paragraph and the preceding one, greatly strengthens their identification as being representative of the samples from which they derive.

As mentioned previously, results show the most variance for the La-containing ceramic. For example, the image obtained by the Oxford group shows a highly ordered state of La at the interface bearing a close resemblance to the case of Sm. Repeated experiments at Oxford have yielded the same result. On the other hand, the image obtained by the LBNL group shows virtually no evidence of La ordering at all. Different still is the image obtained by the ORNL group, which exhibits evidence of additional La sites at the interface not apparent in the image obtained by the Oxford group (although theory identifies the third La site as far more weakly bonding than the other two (A and B) on which there is agreement [22]). Because the three research groups obtained images of specimens derived from the very same La-containing ceramic, the inconsistencies mentioned above cannot be attributed to differences in ceramic composition or processing parameters. Suffice it to say that the results obtained for the La sample, as presented by the three research groups, are ambiguous at present, and further investigation is required.

Although a nitrogen-terminated prismatic surface is often assumed in DFT modelling of these interfaces [22, 26, Dwyer and Nguyen-Manh, Unpublished 2004], there is also experimental evidence suggesting that oxygen termination is present, which may play a role in the observed Ln positions. Attempts to perform EELS measurements to identify the individual bonding characteristics at each Ln site were difficult, primarily because the specimen is electron beam sensitive and atoms were knocked out of their specific atomic positions before the measurement could be made. Nevertheless, the Sm-containing ceramic was the least beam sensitive and allowed this EELS measurement to be performed [23]. Figure 2 shows the Si-L_{23} and Sm-N_{45} near-edge structures, measured at the identified Sm sites (A and B) along the interface. While the Sm-N_{45} near-edge structure at sites A and B is the same, which suggests that the atomic bonding of Sm is the same at each location, there are significant changes in the Si-L_{23} near-edge structure. The Si-L_{23} near-edge structure at site A contains a double peak (102 eV and 103.5 eV). The first of these peaks coincides with measurements taken from bulk Si_3N_4 and is therefore associated with a Si–N bond.

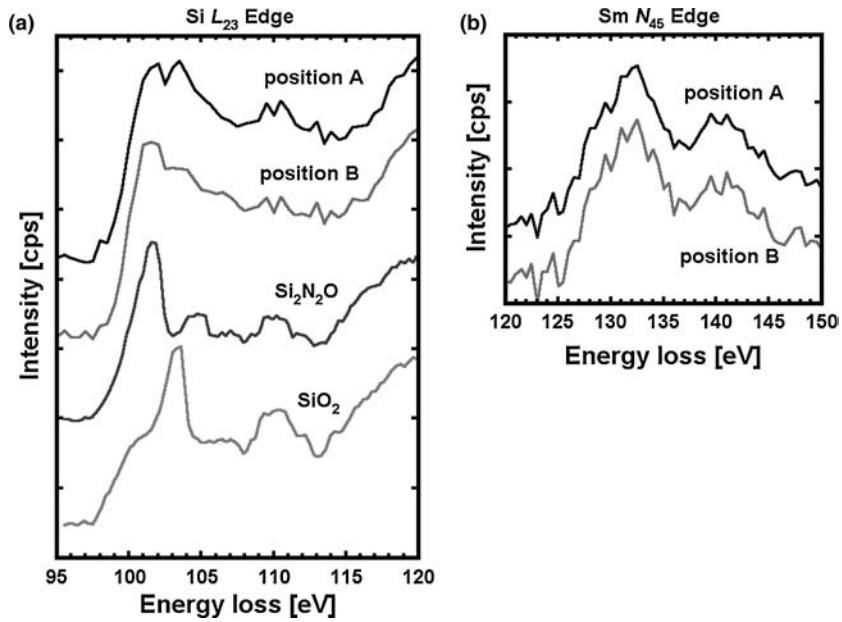

Fig. 2 The EELS results for (**a**) the Si-L_{23} and (**b**) the Sm-N_{45} edges, identifying the individual bonding characteristics at positions A and B. The Si-L_{23} edge shows a double peak at position A but not at position B. This double peak is associated with the presence of oxygen

Identification of the second peak is made by comparison with reference spectra obtained from SiO_2 and Si_2N_2O (two phases commonly encountered during Si_3N_4 ceramic processing). Accordingly, the peak in question is associated with a Si $\neq$ O bond because its position in the spectrum closely coincides with measurements taken on SiO_2. This suggests that at least some of the terminating anions on the Si_3N_4 prism plane at site A are oxygen. In contrast, the Si-L_{23} near-edge structure at site B suggests the presence of nitrogen and shows little evidence of oxygen. The presence of oxygen termination is also supported by grand canonical Monte Carlo simulations of intergranular films in silicon nitride [32], in which a significant proportion of what were initially terminating nitrogen atoms get replaced with oxygen, driven by the energetics to reduce the number of under coordinated terminating nitrogen atoms. However, the preliminary experimental data shown here is available only for the Sm-containing ceramic and further investigation is required.

The presence of interfacial steps, which potentially complicates the interpretation of images such as those presented in Fig. 1, warrants discussion. Atomically flat prismatic interfaces were routinely observed to persist for at least several tens of nanometers by all three research groups. An example of such an interface in the Lu-containing sample is shown in Fig. 3. Although this interface bounds an

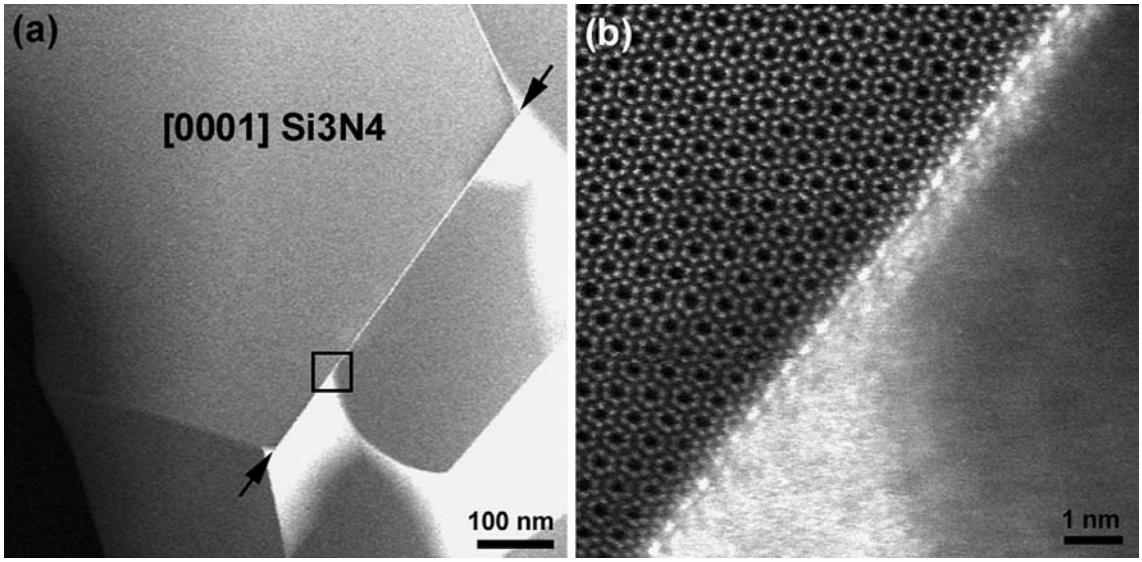

Fig. 3 (**a**) ADF-STEM image of an atomically flat prismatic interface (indicated by arrows) bounding an intergranular film and triple pockets in Lu-containing silicon nitride. The amorphous silicon oxynitride appears bright due to the presence of Lu, while the vacuum in the lower-left corner appears black. (**b**) High-resolution image of the area indicated in (**a**)

intergranular film in some parts, and a triple pocket in others, it is nevertheless atomically flat along its entire length of approximately 0.5 μm. Such behaviour is often observed and demonstrates the high likelihood of finding prismatic interfaces which are step-free throughout the field of view. When steps in prismatic interfaces *were* observed, it was almost always when the interface bounded an intergranular film, i.e. the presence of another Si_3N_4 grain impeded growth of the prism plane. When such steps intersect the surfaces of the specimen, which is often the case, they are easily avoided and hence do not pose much of a problem for the analysis of Ln sites. More problematic are interfacial steps that do not intersect the surfaces of the specimen, i.e. buried steps running perpendicular to the electron beam. Because ADF-STEM images are representative of the atomic structure projected along the direction of the electron beam, positions of incomplete silicon columns associated with a buried step could potentially be confused with Ln positions. An example of a buried step in the Yb-containing sample is shown Fig. 4, where, for the purpose of clarity, the image has been periodically averaged using the method described by Winkelman et al. [24, 25]. In this image, Yb atoms are superimposed on the last row of complete hexagons formed by the silicon columns in Si_3N_4. This geometry is exactly what is expected for a buried step comprised of one unit cell of Si_3N_4. Buried steps of this nature are uncommon and, with experience, relatively easily identified and avoided.

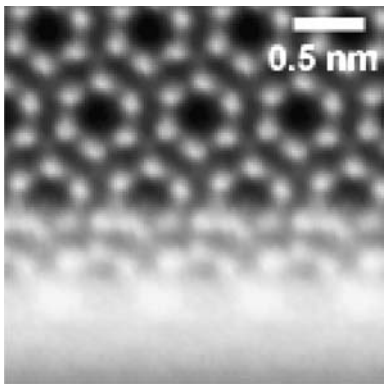

Fig. 4 Periodically averaged ADF-STEM image of a buried step in Yb-containing silicon nitide. The step is comprised of one unit cell of silicon nitride. The positions of Yb are seen superimposed over the silicon nitride structure (cf. Fig. 1)

Conclusion

This work presented a comparison of the ADF-STEM images of interfaces in Ln-containing silicon nitride which were independently obtained by the research groups at Oxford, LBNL and ORNL. It was demonstrated that the vast majority of results obtained by the three research groups are consistent. The images reveal the presence of well-defined Ln segregation sites at the interfaces, and show that these segregation sites are element-specific. In the particular case of the La-containing ceramic, the results, as presented by the three research groups, are somewhat ambiguous, and further investigation is required to resolve the differences.

Acknowledgments The group at the University of Oxford acknowledges financial support from the European Community Growth Program under the NANOAM project (Contract No. GRD2-200-3030351) in collaboration with the NSF Award (DMR-0010062). Thanks are also due to I. Tanaka for supplying the undoped silicon nitride sample, and R. M. Cannon for many useful suggestions and stimulating discussions. The group at Lawrence Berkeley National Laboratory acknowledges the financial support by the Director, Office of Science, Office of Basic Energy Sciences, Division of Materials Sciences and Engineering of the U.S. Department of Energy Department of Energy under Contract No. DE-AC03-76SF00098, DE-AC02-05CH11231 and FG02-03ER-46057. We also would like to thank Dr. R. M. Cannon for helpful discussions. ORNL participants PFB, GSP and SJP acknowledge financial support by the US Department of Energy, Office of Basic Energy Sciences, Division of Materials Sciences and Engineering under contract DE-AC05-00OR22725 with UT-Battelle, LLC.

References

1. Wiederhorn SM (1984) Ann Rev Mater Sci 14:373
2. Ritchie RO (1988) Mater Sci Eng A 103:15
3. Becher PF (1991) J Am Ceram Soc 74:255
4. Clarke DR (1994) In: Hoffmann MJ, Petzow G (eds) Tailoring of mechanical properties of Si_3N_4 ceramics, NATO ASI Series. Kluwer Academic Publishers, p 291
5. Lawn BR (1993) Fracture of brittle solids, 2nd edn. Cambridge University Press, pp Ch 8
6. Swanson PL, Fairbanks CJ, Lawn BR, Mai Y-W, Hockey BJ (1987) J Am Ceram Soc 70:279
7. Mai Y-W, Lawn BR (1987) J Am Ceram Soc 70:289
8. Rödel J, Kelly JF, Lawn BR (1990) J Am Ceram Soc 73:3313
9. Maniette Y, Inagaki M, Sakai M (1991) J Euro Ceram Soc 7:255
10. Bennison SJ, Lawn BR (1989) Acta Metall Mater 37:2659
11. Li C-W, Yamanis J (1989) Ceram Eng Sci Proc 10:632
12. Li C-W, Lee D-J, Lui S-C (1992) J Am Ceram Soc 75:1777
13. Vekinis G, Ashby MF, Beaumont WR (1990) Acta Metall Mater 38:1151
14. Reichl A, Steinbrech RW (1988) J Am Ceram Soc 71:C299
15. Becher PF (1991) In: Shah SP (ed) Toughening mechanisms in quasi-brittle materials. Kluwer Academic Publishers, p 19
16. Kawashima T, Okamoto H, Yamamoto H, Kitamura A (1991) J Ceram Soc Japan 99:320
17. Dauskardt RH (1993) Acta Metall Mater 41:2765
18. Sajgalik P, Susza J, Hoffmann MJ (1995) J Am Ceram Soc 78:2619
19. Hoffmann MJ, Petzow G (1993) Mater Res Soc Symp Proc 287:3
20. Petzow G, Herrmann M (2002) In: Jansen M, Mingos DMP (eds) High performance non-oxide ceramics II. Springer-Verlag, Berlin
21. Sun EY, Becher PF, Hsueh C-H, Painter GS, SB Waters S-L Hwang, Hoffmann MJ (1999) Acta Mater 47:2777
22. Shibata N, Pennycook SJ, Gosnell TR, Painter GS, Shelton WA, Becher PF (2004) Nature 428:730
23. Ziegler A, Idrobo JC, Cinibulk MK, Kisielowski C, Browning ND, Ritchie RO (2004) Science 306:1768

24. Winkelman GB, Dwyer C, Hudson TS, Nguyen-Manh D, Döblinger M, Satet RL, Hoffmann MJ, Cockayne DJH (2004) Phil Mag Lett 84:755
25. Winkelman GB, Dwyer C, Hudson TS, Nguyen-Manh D, Döblinger M, Satet RL, Hoffmann MJ, Cockayne DJH (2005) Appl Phys Lett 87:061911
26. Shibata N, Painter GS, Satet RL, Hoffmann MJ, Pennycook SJ, Becher PF (2005) Phys Rev B 72:140101
27. Satet RL, Hoffmann MJ (2005) J Am Ceram Soc 88:2485
28. Satet RL, Hoffmann MJ (2004) J Euro Ceram Soc 24:3437
29. Hoffmann MJ, Gu H, Cannon RM (2000) In: Carter CB, Hall EL, Briant CL, Nutt S (eds) Mater Res Soc Symp Proc 586:65
30. Painter GS, Becher PF, Shelton WA, Satet RL, Hoffmann MJ (2004) Phys Rev B 70:144108
31. Hoffmann MJ, Geyer A, Oberacker R (1999) J Eur Ceram Soc 19:2359
32. Hudson TS, Nguyen-Manh D, van Duin ACT, Sutton AP (2006) Mater Sci Eng A (in press)